



Article

Raindrop Size Distributions of North Indian Ocean Tropical Cyclones Observed at the Coastal and Inland Stations in South India

Balaji Kumar Seela ^{1,†}, Jayalakshmi Janapati ^{1,†}, Chirikandath Kalath Unnikrishnan ², Pay-Liam Lin ^{1,3,4,*}, Jui Le Loh ¹, Wei-Yu Chang ¹, Utpal Kumar ⁵, K. Krishna Reddy ⁶, Dong-In Lee ^{7,8} and Mannem Venkatrami Reddy ⁹



Citation: Seela, B.K.; Janapati, J.; Kalath Unnikrishnan, C.; Lin, P.-L.; Le Loh, J.; Chang, W.-Y.; Kumar, U.; Reddy, K.K.; Lee, D.-I.; Venkatrami Reddy, M. Raindrop Size Distributions of North Indian Ocean Tropical Cyclones Observed at the Coastal and Inland Stations in South India. *Remote Sens.* **2021**, *13*, 3178. <https://doi.org/10.3390/rs13163178>

Academic Editors: Sanghun Lim and Shaik Allabakash

Received: 23 June 2021

Accepted: 3 August 2021

Published: 11 August 2021

Publisher's Note: MDPI stays neutral with regard to jurisdictional claims in published maps and institutional affiliations.



Copyright: © 2021 by the authors. Licensee MDPI, Basel, Switzerland. This article is an open access article distributed under the terms and conditions of the Creative Commons Attribution (CC BY) license (<https://creativecommons.org/licenses/by/4.0/>).

- ¹ Department of Atmospheric Sciences, Institute of Atmospheric Physics, National Central University, Zhongli District, Taoyuan City 320317, Taiwan; seelabalaji@pblap.atm.ncu.edu.tw (B.K.S.); lakshmijaya2009@pblap.atm.ncu.edu.tw (J.J.); haidyloh@g.ncu.edu.tw (J.L.L.); wychang@g.ncu.edu.tw (W.-Y.C.)
 - ² National Centre for Earth Science Studies, ESSO-MoES, Government of India, Akkulam, Thiruvananthapuram 695 011, India; unnikrishnan.ck@ncss.gov.in
 - ³ Earthquake-Disaster & Risk Evaluation and Management Center, National Central University, Zhongli District, Taoyuan City 320317, Taiwan
 - ⁴ Research Center for Hazard Mitigation and Prevention, National Central University, Zhongli District, Taoyuan City 320317, Taiwan
 - ⁵ Institute of Earth Sciences, Academia Sinica, Taipei 11529, Taiwan; utpalkumar@earth.sinica.edu.tw
 - ⁶ Semi-Arid Zonal Atmospheric Research Centre, Department of Physics, Yogi Vemana University, Kadapa 516002, India; kkrreddy@yogivemanauniversity.ac.in
 - ⁷ Department of Environmental Atmospheric Sciences, Pukyong National University, Busan 48513, Korea; leedi@pknu.ac.kr
 - ⁸ Atmospheric Environmental Research Institute, Pukyong National University, Busan 48513, Korea
 - ⁹ National Centre for Medium Range Weather Forecasting, Ministry of Earth Sciences, Noida 201309, India; venkat@ncmrwf.gov.in
- * Correspondence: tliam@pblap.atm.ncu.edu.tw
† Balaji Kumar Seela and Jayalakshmi Janapati contributed equally to this work.

Abstract: The current study summarizes the raindrop size distributions (RSDs) characteristic of the North Indian Ocean (NIO) tropical cyclones (TCs) measured with ground-based disdrometers installed at the coastal (Thiruvananthapuram, 8.5335°N, 76.9047°E) and inland (Kadapa, 14.4742°N, 78.7098°E) stations in south India. The NIO TCs observed at the coastal station showed more mid- and large-size drops (>1 mm) than the inland station. On the other hand, for both inland and coastal stations, small and mid-size drops (<3 mm) primarily contributed to the total number concentration and rainfall rate. The RSDs of the NIO TCs segregated into precipitation types (stratiform and convective) demonstrated the presence of more mid- and large-size drops at the coastal station. The RSD relations of the NIO TCs, which are used in rain retrieval algorithms of remote sensing (global precipitation measurement) radars, exhibited contrasts between the coastal and inland station. Further, the NIO TCs' rainfall kinetic energy relations, which are crucial in rainfall erosivity studies, estimated for the coastal station revealed dissimilar characteristics to that of the inland station. The conceivable thermo-dynamical and microphysical processes that are accountable for the disparities in the NIO TCs RSDs measured at the coastal and inland stations are also elucidated in this work.

Keywords: raindrop size distributions (RSDs); disdrometer; North Indian Ocean (NIO); tropical cyclones (TCs); rainfall kinetic energy; rainfall rate

1. Introduction

Raindrop size distribution (RSD) information from the ground-based disdrometers has profound applications in meteorology, hydrology, and rain attenuation studies. For

instance, knowledge about the RSD is useful in offering accurate RSD models for satellite-borne remote-sensing radar and ground-based weather radar rain-retrieval algorithms [1,2]. Moreover, rainfall kinetic energy-intensity relations computed from the RSDs are useful in evaluating rainfall erosivity factor, one of the key parameters of soil erosion calculation [3,4].

The RSDs show distinct features with respect to different seasons [5–7], weather systems (thunderstorms, frontal systems, and tropical cyclones (TCs)) [8–10], geographical location [11–13], and types of precipitation [14,15]. The substantial vulnerabilities caused by the TCs require us to understand their microphysical attributes, especially the RSDs, which can affect TCs' rainfall estimation algorithms and cloud modeling [16,17].

In terms of understanding the microphysical features of TCs, globally, there has been increasing interest in TC RSD studies. There have been attempts in understanding TCs' RSD features over the Atlantic Ocean [17], Northwest Pacific Ocean [18–21], and South Indian Ocean [22] using ground-based disdrometers, and these studies were conducted using Joss–Waldvogel disdrometer [17,22], 2-Dimensional video disdrometer [20], and Parsivel disdrometer [18,19,23] measurements. Furthermore, over the North Indian Ocean (NIO), the disparities in the RSDs of TC rainfall to the monsoon rainfall, one TC to another TC, as well as between their pre- and post-landfall were well documented [8,9,24,25].

There have been studies on the rainfall characteristics of NIO TCs using remote sensing and model simulations [26,27]. Moreover, previous researchers demonstrated substantial variations in the seasonal rainfall RSDs measured between the coast and inland stations [28–31]. However, there have been no such studies documented for the TCs, especially for the NIO TCs, which led us to conduct the present work with the following questions: 1) do the RSDs of NIO TCs exhibit similar/dissimilar characteristics if they are measured at the coastal and inland station? 2) If there are any disparities in the RSDs of the NIO TCs at the coastal and inland sites, what could be the conceivable microphysical processes responsible for such disparities? 3) In assessing the rainfall estimation algorithms, do we need to adopt unique/different RSDs empirical relations at the coastal and inland sites? 4) do the rainfall kinetic energy—intensity relations, which are worthwhile in soil erosion studies, readily available at the existing literature are adequate to estimate the rainfall kinetic energy of the NIO TCs? Moreover, while assessing the rainfall kinetic energy, do we need to adopt same/different rainfall kinetic energy empirical relations for the NIO TCs at the coastal and inland locations? To answer the above-mentioned question, the present study is carried out by collecting the RSDs of the NIO TCs rainfall at the coastal (Thiruvananthapuram) and inland (Kadapa) sites in south India using ground-based disdrometers.

With this introduction, this article is prepared as follows. Section 2 details the data and methods used, Section 3 provides the results on RSDs features of the NIO TCs measured at the coastal and inland sites, followed by discussion in Section 4, and the summary and conclusions are given in Section 5.

2. Data and Methods

2.1. Tropical Cyclones

In the current study, the RSDs of eight NIO TCs (observed during 2010 to 2018) were measured with first-generation Parsivel (version 1) disdrometers installed at the inland (Kadapa, 14.4742°N, 78.7098°E, 138 m msl) and coastal (Thiruvananthapuram, 8.5335°N, 76.9047°E, 15 m msl) stations in south India. Among eight NIO TCs, four TCs (Jal-2010: 07–08 November 2010, Depression-2010: 06–08 December 2010, Nilam-2012: 31 October 2012, Depression-2013: 16–17 November 2013) were measured at the inland station, and the remaining four (Deep Depression-2011: 26–27 November 2011, Ockhi-2017: 30 November–02 December 2017, Depression-2018: 13–14 March 2018, Gaja-2018: 16 November 2018) at the coastal station. The track information of the selected eight NIO TCs is archived from the India Meteorological Department. The tracks of selected eight NIO TCs and the locations of the disdrometers installed at the inland and coastal stations (denoted with red squares) are shown in Figure 1.

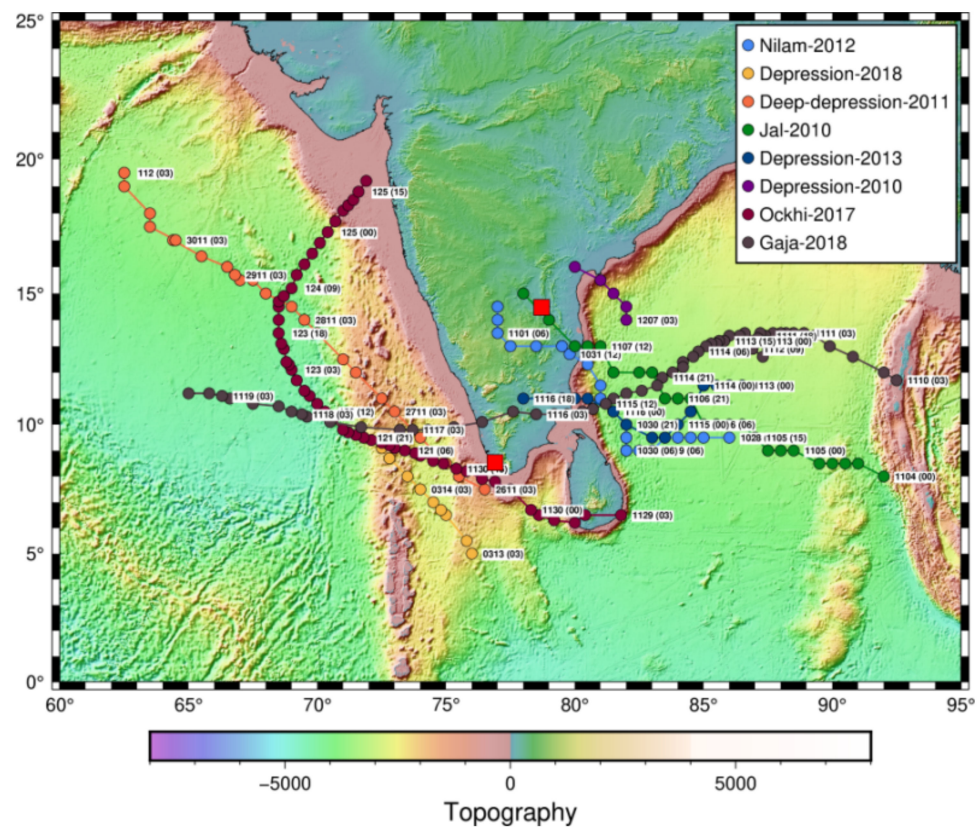


Figure 1. Tracks of selected NIO TCs. The disdrometers' sites are denoted with red square boxes. Along the tracks, the date and time of each TC is denoted in the form of MonthDay (hours).

2.2. Parsivel Disdrometer

The Parsivel [32,33] disdrometer can measure liquid (0.2–5 mm) and solid (0.2–25 mm) precipitating particles, their velocity (0.2–20 ms^{-1}), and records them in a raindrop size and velocity matrix of 32 by 32. The Parsivel uses 650 nm laser beam (length, width, and height of 180 mm, 30 mm, and 1 mm, respectively) and 3 mW power. The basic working principle and pros and cons of the Parsivel were detailed by Löffler–Mang and Joss [33], Battaglia et al. [34], Jaffrain and Berne [35], Friedrich et al. [36], and Tokay et al. [37]. The Parsivel is prone to some instrumental errors, such as marginal effect and splashing effect. To overcome these limitations, quality-control procedures, mentioned below were applied to the RSD measurements of the disdrometers in the inland and coastal sites. In the present work, the first two size bins of disdrometer are not considered in the RSD computations, and the RSD samples with rainfall rate $< 0.1 \text{ mm h}^{-1}$ were removed from the analysis [38]. Moreover, drops of diameter $> 6 \text{ mm}$ and fall speeds with $\pm 60\%$ of fall velocity-diameter relation were discarded [35,39].

The raindrop concentration ($N(D_i)$, $\text{m}^{-3} \text{ mm}^{-1}$) of NIO TCs is estimated using below calculation [36,37].

$$N(D_i) = \sum_{i=1}^{32} \sum_{j=1}^{32} \frac{n_{ij}}{A_{eff} \Delta t V(D_i) \Delta D_i} \quad (1)$$

where drops measured in drop size bin ' i ' and velocity bin ' j ' are denoted with n_{ij} . Sampling time, effective sampling area, terminal velocity of the raindrops, and i^{th} drop diameter class width are represented, respectively, with Δt ($= 60 \text{ s}$), A_{eff} (m^2) [$= 10^{-6} \times L \left(B - \frac{D_i}{2} \right) \text{ m}^2$], L ($= 180 \text{ mm}$), B ($= 30 \text{ mm}$), $V(D_i)$ ($= 9.65 - 10.3 e^{-0.6 * D_i}$, m s^{-1}), and ΔD_i (mm) [33,34,37,39].

The integral RSD parameters, like radar reflectivity (Z), rainfall rate (R), total number concentration (N_t), and liquid water content (W) are expressed as:

$$Z \text{ (dBZ)} = 10 \log_{10} \sum_{i=1}^{32} \sum_{j=1}^{32} D_i^6 \frac{n_{ij}}{A_{eff} \Delta t V(D_i)} \quad (2)$$

$$R \text{ (mm h}^{-1}\text{)} = 6\pi \times 10^{-4} \sum_{i=1}^{32} \sum_{j=1}^{32} D_i^3 \frac{n_{ij}}{A_{eff} \Delta t} \quad (3)$$

$$N_t \text{ (m}^{-3}\text{)} = \sum_{i=1}^{32} \sum_{j=1}^{32} \frac{n_{ij}}{A_{eff} \Delta t V(D_i)} \quad (4)$$

$$W \text{ (g m}^{-3}\text{)} = \frac{\pi}{6} \times 10^{-3} \rho_w \sum_{i=1}^{32} \sum_{j=1}^{32} D_i^3 \frac{n_{ij}}{A_{eff} \Delta t V(D_i)} \quad (5)$$

The water density is denoted with ρ_w , which is equal to 1 g cm^{-3} .

The gamma distribution function as given below is fitted with the NIO TCs RSDs measured at the coast and inland [40]:

$$N(D) = N_0 D^\mu \exp(-\Lambda D) \quad (6)$$

here, N_0 is the intercept parameter ($\text{m}^{-3} \text{ mm}^{-1-\mu}$), μ is shape parameter (-), and λ is the slope parameter.

The intercept parameter N_0 is given by [41]:

$$N_0 = \frac{\lambda^{\mu+4} M_3}{\Gamma(\mu+4)} \quad (7)$$

The RSD n^{th} moment, M_n ($\text{mm}^n \text{ m}^{-3}$) is given as

$$M_n = \int_{D_{min}}^{D_{max}} D^n N(D) dD \quad (8)$$

The above equation can provide the 3rd, 4th, and 6th moments of the RSDs if $n = 3, 4$, and 6 , respectively.

From the three moments (M_3, M_4 , and M_6), D_m (mass-weighted mean diameter, mm), μ (shape parameter, -), λ (slope parameter, mm^{-1}), and N_w (normalized intercept parameter, $\text{mm}^{-1} \text{ m}^{-3}$) can be expressed as [40,42,43].

$$D_m = \frac{M_4}{M_3} \quad (9)$$

$$\mu = \frac{(11G - 8) + \sqrt{G(G + 8)}}{2(1 - G)} \quad (10)$$

where G is

$$G = \frac{M_4^3}{M_3^2 M_6} \quad (11)$$

$$\Lambda = \frac{(\mu + 4) M_3}{M_4} \quad (12)$$

$$N_w = \frac{4^4}{\pi \rho_w} \left(\frac{10^3 W}{D_m^4} \right) \quad (13)$$

Apart from the above-mentioned meteorological parameters, we evaluated the rainfall kinetic energy relations for the NIO TCs. The rainfall kinetic energy expenditure (KE_{time} , $J m^{-2} h^{-1}$) and the rainfall kinetic energy content (KE_{mm} , $J m^{-2} mm^{-1}$) are expressed as [44]:

$$KE_{time} (J m^{-2} h^{-1}) = \left(\frac{\pi}{12}\right) \left(\frac{1}{10^6}\right) \left(\frac{3600}{t}\right) \left(\frac{1}{A_{eff}}\right) \sum_{i=1}^{32} n_i D_i^3 [V(D_i)]^2 \quad (14)$$

$$KE_{mm} (J m^{-2} mm^{-1}) = \left(\frac{KE_{time}}{R}\right) \quad (15)$$

where, R is the rainfall intensity in $mm h^{-1}$.

2.3. Reanalysis Data

Along with the disdrometer measurements, convective available potential energy (CAPE) ($J Kg^{-1}$), vertical integral of water vapor ($Kg m^{-3}$), air temperature and relative humidity profiles from the European Centre for Medium-Range Weather Forecasts interim re-analysis are adopted [45].

3. Results

The quality-controlled data of the Parsivel disdrometers showed 3901 and 3715 1-min RSD samples of the NIO TCs, respectively, at the coastal (Thiruvananthapuram) and inland (Kadapa) stations. Distributions of mean raindrop concentrations for the coast and inland stations are shown in Figure 2. In the current study, drops of diameter <1 mm, 1 mm to 3 mm, and >3 mm [8,9,17,25] are classified as small-, mid-, and large-size drops, respectively. The concentration of the raindrops above 1 mm diameter is greater for the coastal station than the inland station. Examination of the coast and inland stations' RSDs for different TCs intensities (depression, deep depression, cyclonic storm, and severe cyclonic storm) also showed raindrops above 1 mm diameter are more at the coastal station than the inland station (figure not shown). The NIO TCs at the coastal station are found to have higher R ($mm h^{-1}$), D_m (mm), and lower $\log_{10} N_w$ (N_w in $mm^{-1} m^{-3}$) values than the inland station (Figure 2). Larger D_m values at the coastal station are due to the presence of more mid- and large-size drops than the inland station.

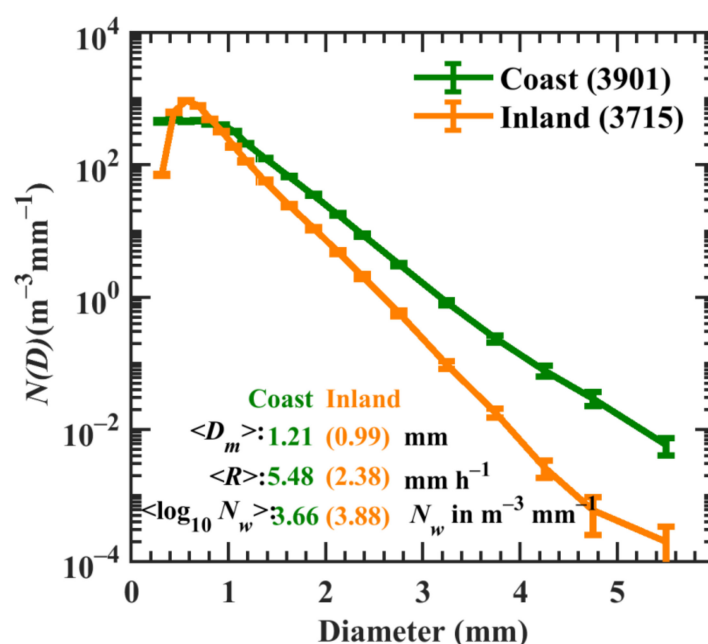


Figure 2. Variations in mean raindrop concentration, $N(D)$ ($mm^{-1} m^{-3}$) of the NIO TCs measured at the coastal and inland stations.

Previously reported D_m and $\log_{10}N_w$ values for the TCs measured at different parts of the globe are given in Table 1 [10,12,17,18,20,22,23,46,47]. Owing to geographical variations or different types of disdrometers, the D_m values of other oceanic TCs are different from those of the NIO TCs measured at the coastal and inland stations. If we compare the NIO TCs' D_m and N_w values with those of the Northwest Pacific Ocean TCs, it is obvious that NIO TCs have smaller (larger) D_m (N_w) values. The presence of more convective clouds in the Northwest Pacific Ocean TCs than the NIO TCs could be the reason for the occurrence of more large-size drops in the Northwest Pacific Ocean TCs [18].

Table 1. Mean D_m and $\log_{10}N_w$ values of the NIO TCs. The Atlantic Ocean, North Indian Ocean, North West Pacific, South Indian Ocean, are denoted, respectively, with AO, NIO, NWP, SIO. The Joss–Waldvogel disdrometer and 2-Dimensional video disdrometer are denoted with JWD and 2DVD, respectively.

Ocean	Studies	Observational Location	Instrument	TCs Number	D_m (mm)	$\log_{10}N_w$ ($\text{mm}^{-1} \text{m}^{-3}$)
NIO	Present study	Coast	Parsivel	Four	1.21 ± 0.36	3.66 ± 0.51
NIO	Present study	Inland	Parsivel	Four	0.99 ± 0.34	3.88 ± 0.57
SIO	Deo and Walsh [22]	Darwin, Australia	JWD	Seven	1.75	-
NWP	Chang et al. [20]	Zhongli, north Taiwan	2DVD	Fourteen	2	3.8
	Janapati et al. [18]	Kaohsiung, south Taiwan	Parsivel	Six	1.33 ± 0.39	3.42 ± 0.47
	Chen et al. [23]	Fujian, east China	Parsivel	One	1.30	-
	Wang et al. [46]	Jiangning, eastern China	2DVD	One	1.41	4.67
	Wen et al. [47]	East and south China.	2-DVD	Seven	1.13 ± 0.24	-
	Chen et al. [10]	Tokyo, Japan	JWD	Four	1.25 ± 0.36	3.74 ± 0.47
AO	Le Loh et al. [12]	Miryang, South Korea	Parsivel	Two	1.19	3.44
	Tokay et al. [17]	USA	JWD	Eight	1.67 ± 0.30	-

The variations of $\log_{10}R$, $\log_{10}W$, D_m , and $\log_{10}N_w$ with their probability distribution functions (PDF) for the NIO TCs measured at the coastal and inland stations are depicted in Figure 3. TCs' rainfall at the inland site shows peak rainfall rates distribution at $\log_{10}R = 0$ and at the coastal site shows peak distribution at $\log_{10}R = 0.2$ (Figure 3a). Rainfall rates of the inland site show higher distribution than the coastal station for $\log_{10}R < 0.4$ and for $\log_{10}R > 0.4$ the coastal station showed a higher distribution than the inland station (Figure 3a). The PDF distributions for the liquid water content at the coastal show a relatively greater frequency for $\log_{10}W > -0.76$ than at inland station (Figure 3b). A remarkable difference in the PDF distributions of D_m between the coastal and inland sites can be attributed to more raindrops of diameter > 1 mm at the coast than the inland site (Figure 3c). The inland station's D_m values have peak PDF at 0.98 mm and the coastal station's D_m values have peak PDF around 1.2 mm. Similar to D_m , the $\log_{10}N_w$ also demonstrated distinct dissimilarities in PDF distributions between the coastal and inland sites (Figure 3d). The TCs' rainfall at the coast have higher PDF values for $\log_{10}N_w < 4$ than the inland, and the inland site showed higher PDF values for $\log_{10}N_w > 4.0$ than coastal site (Figure 3d). Furthermore, to corroborate the variations in these four rain parameters of the inland and coastal sites, the statistical student's t -test was conducted at 0.01 and 0.05 significant levels and the test results rejected the null hypothesis confirming that the NIO TCs' rain/RSD parameters at the coast are different from that of the inland site.

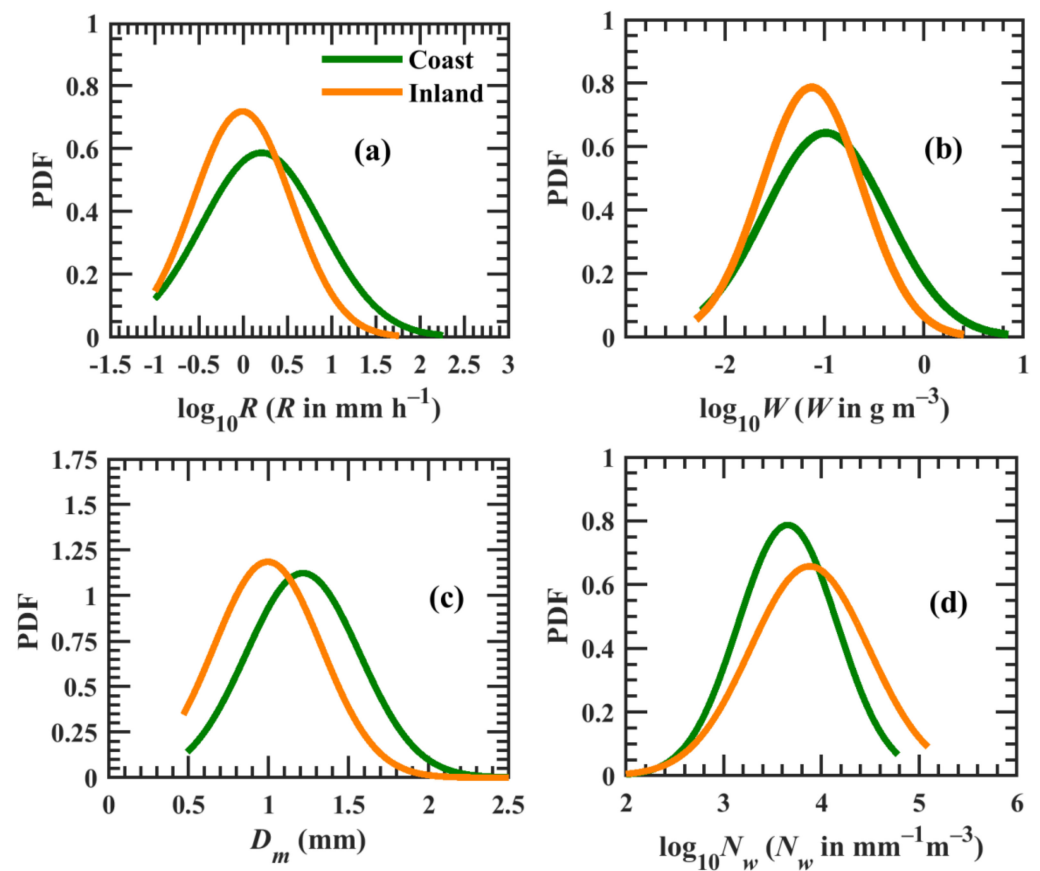


Figure 3. The PDF of (a) $\log_{10}R$, (b) $\log_{10}W$, (c) D_m (mm), and (d) $\log_{10}N_w$ for the NIO TCs measured at the coastal and inland stations.

3.1. Contribution of Raindrop Diameters to N_t and R

To appraise the NIO TCs RSDs variability between the coastal and inland stations, the contribution of drop diameter classes (as shown in x -axis labels of Figure 4) to total number concentration (N_t , m^{-3}) and rainfall rate (R , m h^{-1}) are portrayed in Figure 4. For both the locations (coast and inland), with the increase in drop diameter classes, contribution to total number concentration decreased, while that to rainfall rate increased and then decreased, and this characteristic is alike with the findings of Chen et al. [10] for the Pacific Ocean TCs measured in Japan. Small-size drops predominantly added to a higher N_t ($> 80\%$ and $> 70\%$ for the NIO TCs measured at the inland and coastal stations, respectively) and contributed to about 30% of the rainfall rate at the inland station, and 11% of rainfall rate at the coastal station. The contribution of raindrops with diameters 1–2 mm to number concentration is around 13% (26%), and their contribution to rainfall rate is around 54% (55%) for the NIO TCs measured at the inland (coastal) station. The contribution of drops with diameters 2–3 mm to number concentration is negligible ($< 2\%$ and $< 0.5\%$ for the NIO TCs measured at the coastal and inland stations), and the contribution to rainfall rate is around 13% for the inland station and 25% for the coastal station. Figure 4a,b clearly demonstrates that raindrops with diameter < 3 mm contributed to a higher percentage of total number concentration and rainfall rate for the NIO TCs measured at both stations.

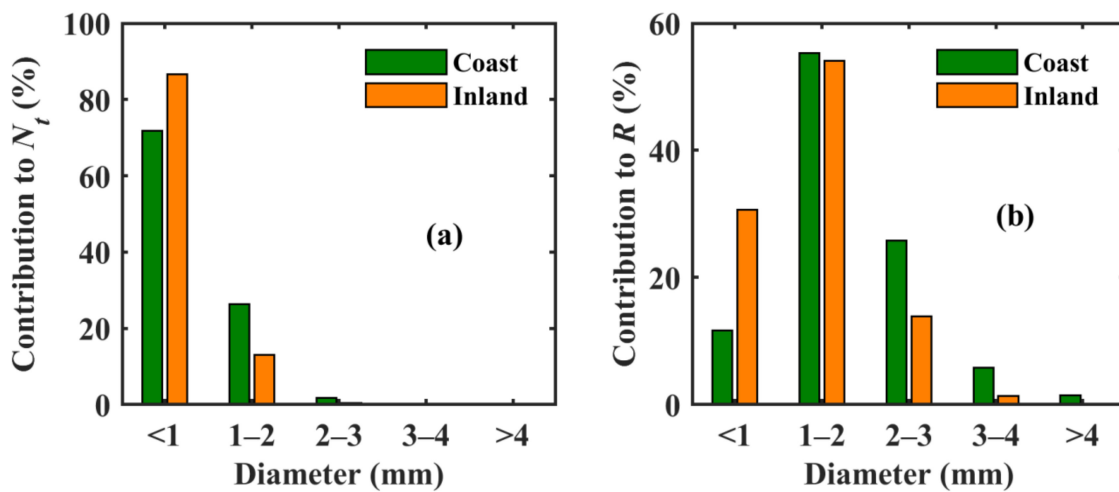


Figure 4. Contribution of drop diameter classes to (a) number concentration, N_t (m^{-3}) and (b) rainfall rate, R (mm h^{-1}) for the NIO TCs measured at the coastal and inland stations.

3.2. RSDs in Precipitation Types

Microphysical characteristics of precipitating clouds were found to vary profoundly with precipitation types (stratiform and convective), which have a major influence on microphysical parameterizations and rainfall retrieval algorithms [42]. There have been reports on different approaches in classifying the rainfall into stratiform and convective types [42,43,48]. We classified the NIO TCs' rainfall at the coastal and inland stations to convective and stratiform type using the classification method of Bringi et al. [43]. If the mean R of 10 successive 1-min RSD samples was $> 5 \text{ mm h}^{-1}$ ($>0.5 \text{ mm h}^{-1}$) and the standard deviation $> 1.5 \text{ mm h}^{-1}$ ($<1.5 \text{ mm h}^{-1}$), then those samples were considered as convective (stratiform) type. With the above-mentioned classification criteria, 64% (36%) of data points are stratiform (convective) type for the NIO TCs at the coastal station, and they contributed to 15% (85%) rainfall accumulation, respectively. For the NIO TCs at the inland station, around 85% (15%) of data points are stratiform (convective) type, and they contributed to rainfall accumulations of 46% (54%), respectively.

Distributions of mean $N(D)$ with raindrop diameters in two precipitation regimes of the NIO TCs at the coastal and inland stations are shown in Figure 5a. For both the coastal and inland stations, a higher number of raindrops greater than 1 mm in diameter was observed for convective regimes than for stratiform regimes. The convective regimes of the inland and coastal stations showed broader distributions than the stratiform regimes, which could be owing to the large drops' collisional breakup in convective regimes [49]. A nearly exponential distribution can be seen for the stratiform RSDs at the coastal region. Furthermore, for both stratiform and convective regimes, the TCs at the coastal station have more raindrops of diameter $> 1 \text{ mm}$ as compared to the inland station. Mean values of mass-weighted mean diameter and normalized intercept parameter in stratiform and convective regimes for the coastal and inland stations are provided in Figure 5b. Compared to stratiform type, the convective type has a larger D_m and $\log_{10}N_w$ values. On the other hand, in both convective and stratiform regimes, larger $\log_{10}N_w$ and smaller D_m values can be seen at the inland as compared to the coastal station. In Figure 5b, the range of $\log_{10}N_w$ and D_m values for the continental and maritime precipitations of Bringi et al. [43] are drawn with rectangular boxes. When comparing present TCs with the precipitation clusters described by Bringi et al. [43], the D_m and $\log_{10}N_w$ distributions have smaller values of D_m than the maritime convective clusters (except in the coastal station convective regime). The $\log_{10}N_w$ values in convective regimes of both locations fell under the maritime convective clusters.

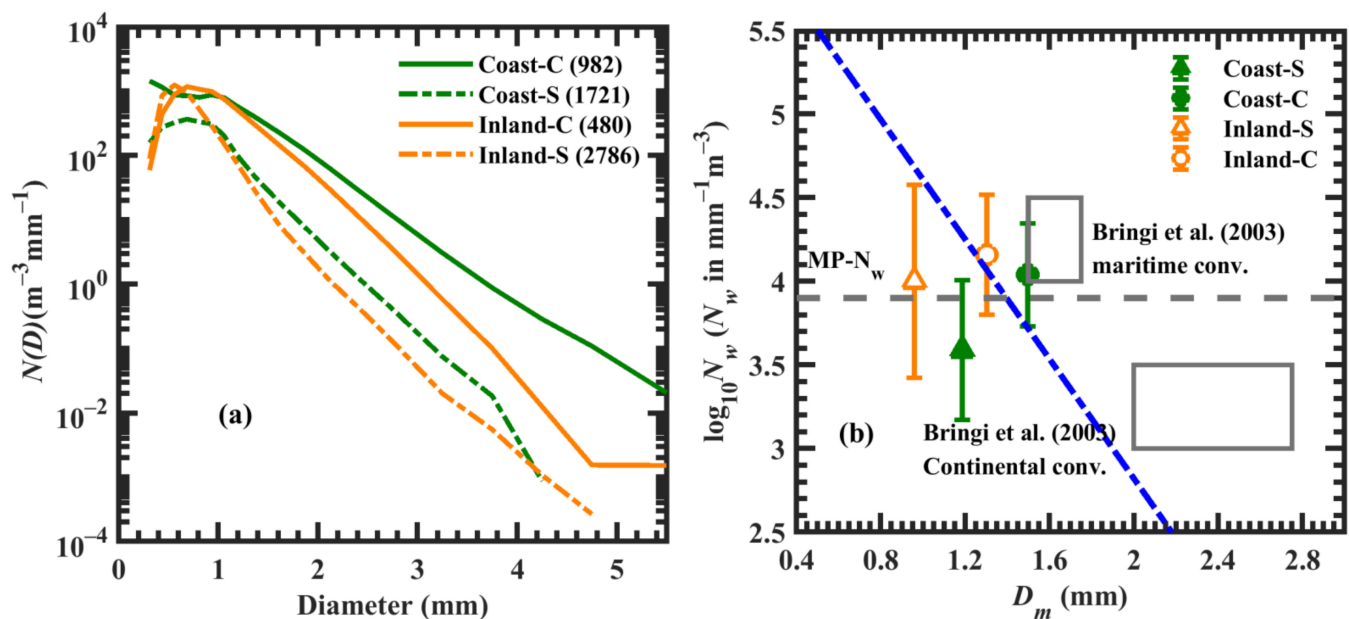


Figure 5. (a) Variations in mean raindrop concentration for stratiform (S) and convective (C) rainfall, and (b) variations of mean $\log_{10}N_w$ with D_m values for convective and stratiform rainfall measured at the coastal and inland stations.

3.3. $D_m - Z_{Ku}/Z_{Ka}$ and $D_m - N_w$ Relations

The GPM DPR that operates at Ka- and Ku-band can provide the radar reflectivities at these two frequencies and are denoted, respectively, as Z_{Ka} and Z_{Ku} . The RSDs (D_m and N_w) and the rainfall parameters for the GPM DPR can be inferred from the difference between the radar reflectivity at two frequency bands, known as the differential frequency ratio (DFR, in dB) [50]. The Z_{Ku} and Z_{Ka} are evaluated from the RSD measurements from the coastal and inland station using T-matrix simulations with 20 °C temperature [51,52]. The scatter plots of DFR with D_m values at the coast and inland are depicted in Figure 6. Parallel to the results reported in the literature, DFR- D_m plots for both the locations showed a “double solution” problem, which leads to the ambiguity in the estimation of D_m [1,50]. This double solution problem arises due to the dominance of Rayleigh scattering at Ka-band and Ku-band reflectivities during the weak rain, which is mostly associated with small-size raindrops [53]. Due to the dual-value problem with DFR, rather than deriving the empirical relations between D_m and DRF, like previous researchers [2,54,55], we evaluated the relations between D_m and effective radar reflectivity values. The distributions of $D_m - Z_{Ku}$, $D_m - Z_{Ka}$, and $\log_{10}N_w - D_m$ and their polynomial fit lines for the coastal and inland stations are illustrated in Figure 7. For both the locations, Z_{Ku}/Z_{Ka} increases with the increase in D_m values. The second-degree polynomial relations ($D_m - Z_{Ka}$, $D_m - Z_{Ku}$, $\log_{10}N_w - D_m$ relations) computed using the non-linear least squares method for the inland and coastal stations are also depicted in Figure 7. The derived D_m relations with Z_{ku} , Z_{ka} , and N_w clearly demonstrate that they differ substantially from the coast to the inland station, which hints at the need to adopt different empirical relations while estimating the DSD parameters for the NIO TCs from the GPM DPR measurements.

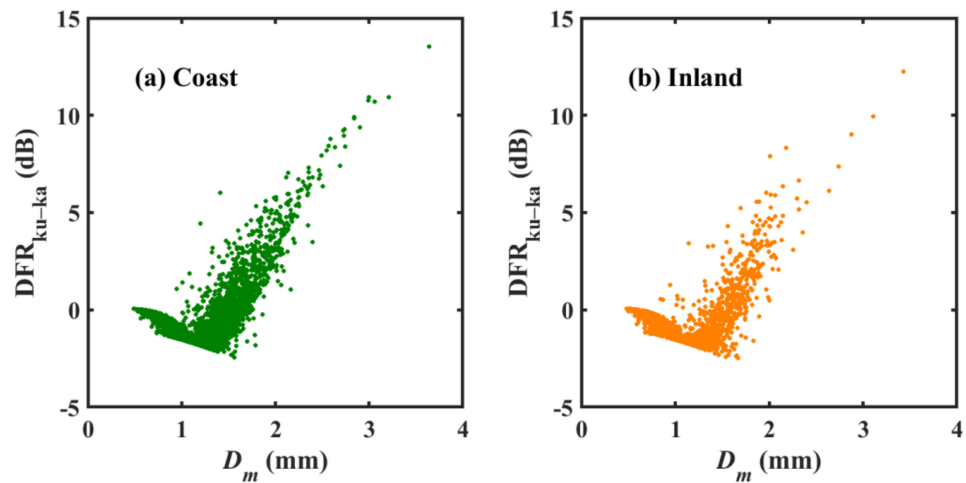


Figure 6. Scatter plot between DFR and D_m (mm) for the NIO TCs measured at the coastal and inland stations.

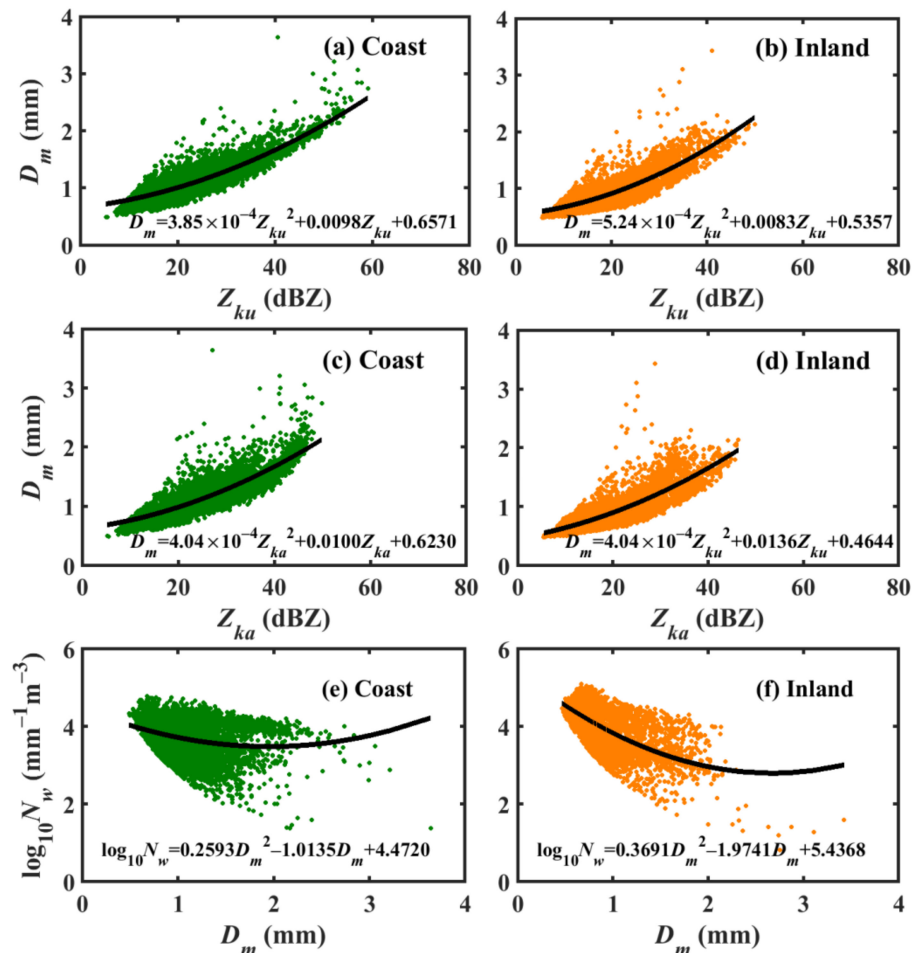


Figure 7. D_m - Z_{ku} , D_m - Z_{ka} , and $\log_{10}N_w$ - D_m relations for the NIO TCs measured at the coastal and inland stations.

3.4. Rainfall Kinetic Energy Relations

Rainfall kinetic energy (KE) is an important parameter in soil erosion studies that is used in estimating the rainfall erosivity factor [56]. Because of the expensive experimental requirement for the direct measurement of rainfall KE , alternative methods have been adopted by previous researchers [57,58]. Alternatively, rainfall KE can be estimated from the RSD

information measured with the disdrometers [44]. For the locations where there is no availability of RSD information, the KE and the rainfall erosivity factor can be estimated using the empirical relations between rainfall KE and rainfall intensity (KE-R relations) [3,59]. These relations showed diversity with the geographical location and weather systems [3,21,60,61], which requires one to deduce region-specific relations. Moreover, in India, due to the lack of indigenous KE relations, previous studies adopted the relations of other areas [62], which can result in overestimation or underestimation of KE. Henceforth, in the present work, for the first time, the NIO TCs rainfall KE relations are obtained in terms of R (rainfall intensity, mm h^{-1}), and D_m (mass-weighted mean diameter, mm).

Distributions of rainfall kinetic energy (KE_{time} and KE_{mm}), with R for the inland and coastal stations are depicted in Figure 8. The relations between KE_{time} and rainfall intensity for the NIO TCs are obtained based on the least square method in power and linear forms. The fit lines and the corresponding equations for power and linear forms are also provided in Figure 8a,b. The coefficients of $KE_{\text{time}}-R$ relations (power law: $KE_{\text{time}} = aR^b$; linear: $KE_{\text{time}} = aR + b$) and their correlation coefficient (R^2), root mean square error (RMSE), and normalized RMSE (NRMSE) for the coastal and inland stations are provided in Table 2. Both the power and linear form of equations fitted well at lower rainfall rates, however, at higher rainfall rates, the power fit line showed better performance than the linear form. Moreover, despite a higher correlation coefficient for power and linear fits, the power law revealed smaller RMSE and NRMSE than the linear form. The empirical relations between the rainfall content (KE_{mm}) and the rainfall intensity (R) are derived in power ($KE_{\text{mm}} = aR^b$), logarithmic ($KE_{\text{mm}} = a + b \log_{10} R$), and exponential ($KE_{\text{mm}} = a [1 - b \exp(-cR)]$) forms for the NIO TCs, and the respective fit lines and equations are illustrated in Figure 8c,d. The statistical parameters of these three forms of equations are provided in Table 2. The present result on the NIO TCs KE-R relations exhibited analogous behavior to those of the previous studies [63,64].

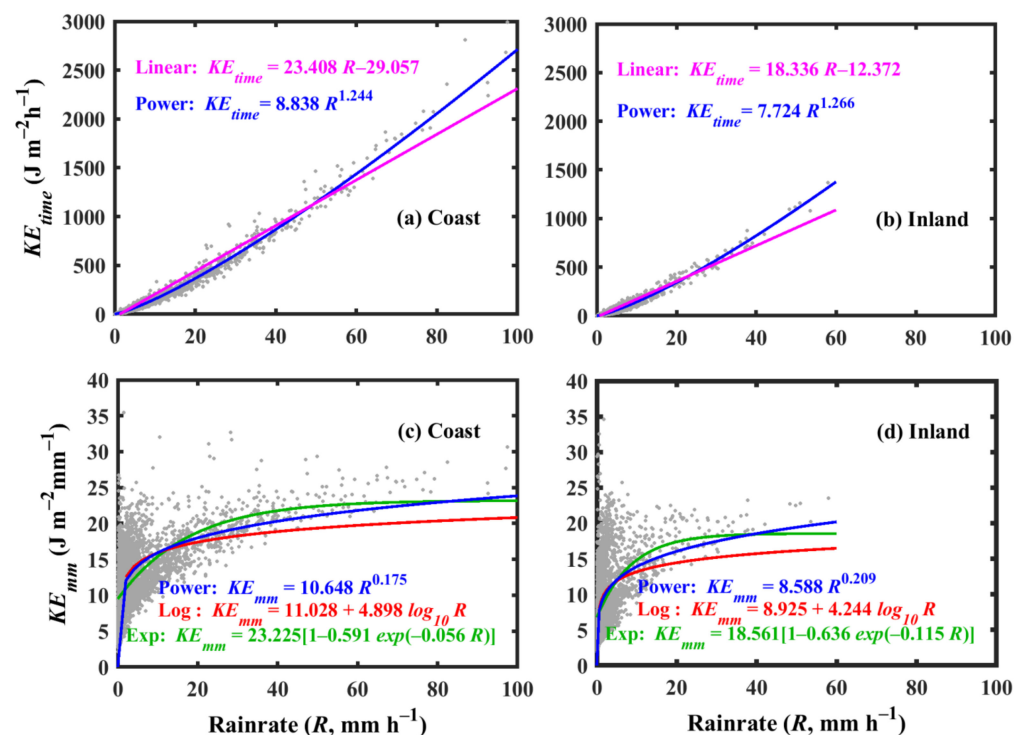


Figure 8. Scatter plots of rainfall kinetic energy (KE_{time} and KE_{mm}) with rainfall rate (R , mm h^{-1}) for the NIO TCs measured at the coastal and inland stations.

With the recent advancements in precipitation measurements from the space, remote-sensing instruments like GPM DPR can provide the radar reflectivity (at ka-band: Z_{ka} and

ku-band: Z_{ku}) and drop size information (mass-weighted mean diameter: D_m) globally [65,66]. By means of empirical relations between rainfall KE and the GPM DPR parameters like D_m , Z_{ka} , and Z_{ku} , one can estimate the rainfall KE at the locations where there are no ground-based measurements. Here, we tried to formulate the empirical relations between rainfall KE and GPM DPR rain parameters (D_m , Z_{ka} , and Z_{ku}), which are depicted in Figures 9 and 10. The empirical relations' values and their statistical parameters for the KE and GPM DPR parameters are given in Table 2. In the KE and D_m distribution plots for the NIO TCs at the coastal and inland station, the second order polynomial equation fits better than the power form. Moreover, the NIO TCs' rainfall kinetic energy expressed in terms of D_m and GPM DPR reflectivities (Z_{ku} and Z_{ka}) showed distinction between the coast and inland stations.

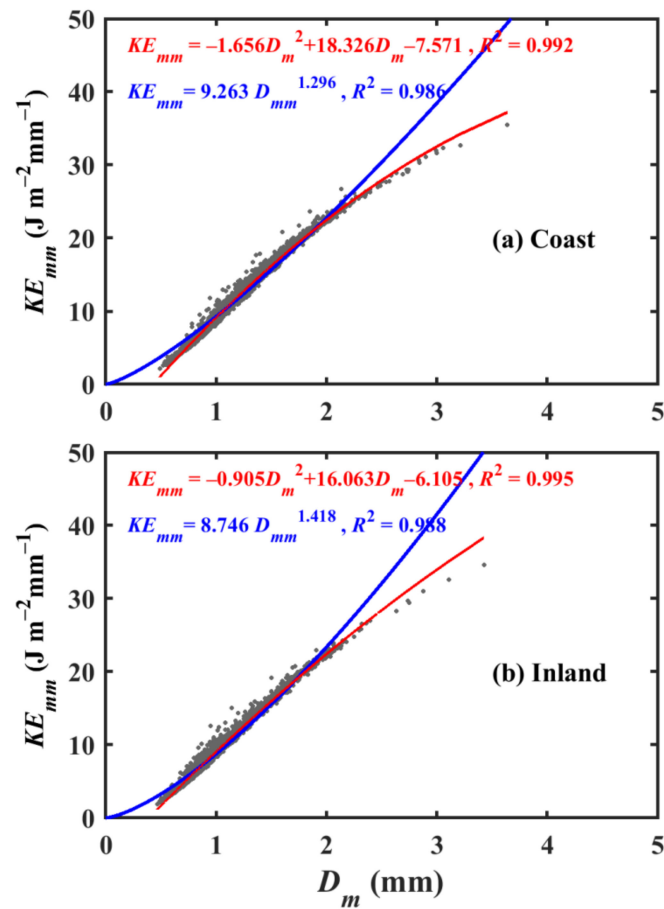


Figure 9. Scatter plots of KE_{mm} and D_m for the NIO TCs measured at the coastal and inland stations.

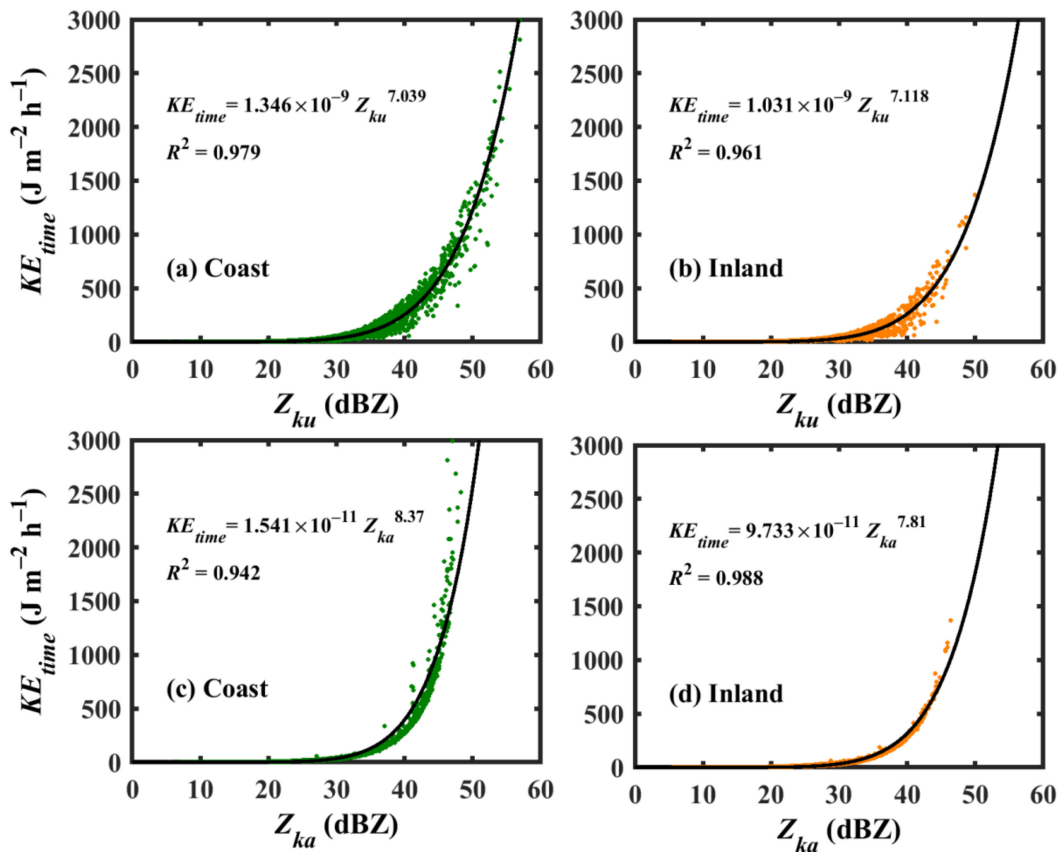


Figure 10. Scatter plots of rainfall kinetic energy with Z_{ku} and Z_{ka} for the NIO TCs measured at the coastal and inland stations.

Table 2. Empirical relations of rainfall kinetic energy (KE_{time} : kinetic energy expenditure/time specific kinetic energy; KE_{mm} : kinetic energy content/volume-specific kinetic energy) with rainfall rate (R , $mm h^{-1}$), mass-weighted mean diameter (D_m , mm), and GPM DPR radar reflectivity (Z_{ku}/Z_{ka} , dBZ).

Region	Fitting	a	b	c	R ²	RMSE	NRMSE	
Coast	$KE_{time}-R$	linear	23.408	-29.057	-	0.979	53.831	0.296
		power	8.838	1.244	-	0.993	30.771	0.169
	$KE_{mm}-R$	power	10.648	0.175	-	0.694	3.535	0.019
		logarithmic	11.028	4.898	-	0.678	3.609	0.02
		exponential	23.225	0.591	0.056	0.678	12.225	0.067
	$KE_{mm}-D_m$	power	9.263	1.296	-	0.986	0.845	0.268
		polynomial	-1.656	18.326	-7.571	0.992	11.745	3.729
Inland	$KE_{time}-Z_{ku}$	power	1.346×10^{-9}	7.039	-	0.979	53.719	0.997
		power	1.541×10^{-11}	8.370	-	0.942	89.286	1.999
	$KE_{time}-R$	linear	18.336	-12.372	-	0.973	20.088	0.347
		power	7.724	1.266	-	0.987	13.904	0.24
		power	8.588	0.209	-	0.52	4.027	0.07
	$KE_{mm}-R$	logarithmic	8.925	4.244	-	0.5	4.081	0.07
		exponential	18.561	0.636	0.115	0.5	10.685	0.185
		power	8.746	1.418	-	0.988	0.766	0.258
	$KE_{mm}-D_m$	polynomial	-0.905	16.063	-6.105	0.995	9.023	3.046
	$KE_{time}-Z_{ka}$	power	1.031×10^{-9}	7.118	-	0.961	24.197	0.544
power		9.733×10^{-11}	7.810	-	0.988	24.197	0.591	

4. Discussion

In order to reveal the conceivable mechanisms that explain the disparities between the coastal and inland stations' RSDs, the CAPE and total column water vapor from the EAR-interim reanalysis are used for the NIO TCs measured at the coastal and inland stations,

and are portrayed in Figure 11. From the figure, it is obvious that the TCs measured at the coast were associated with more water vapor content and strong convection, with stronger updrafts and downdrafts than the inland. Intense convection can enhance the raindrops growth through collision-coalescence and drop sorting processes, and raises the hydrometeors to higher altitudes, which can lead to the possible growth of ice particles (snowflakes) to a larger size (via vapor deposition and aggregation) than at the inland station [43,67]. Drop sorting and intense updrafts can inhibit the small drops from reaching the ground by suspending them aloft, which in turn allows adequate time for collision and coalescence processes leading to the growth of mid-size drops at the expense of small-size drops [49,68]. Furthermore, the vertical profiles of air temperature and relative humidity evidently illustrate that, during the NIO TC measurements, the coastal station had relatively drier conditions than the inland station (Figure 12), and hence, the rate of evaporation of small drops, which were produced through the collision breakup processes, was higher at the coastal station than at the inland station, allowing mostly the mid-size and large drops to reach the surface. The above-stated thermo-dynamical and microphysical processes resulted in more mid- and large-size drops at the coastal station than the inland station, resulting in higher D_m and lower N_w values, as depicted in Figures 2 and 5.

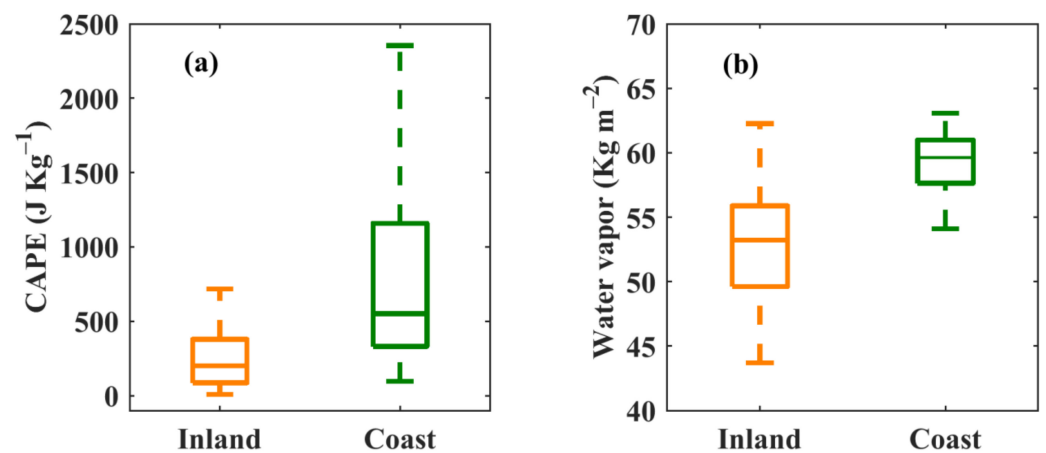


Figure 11. (a) CAPE and (b) vertical integral of water vapor values for the coastal and inland stations.

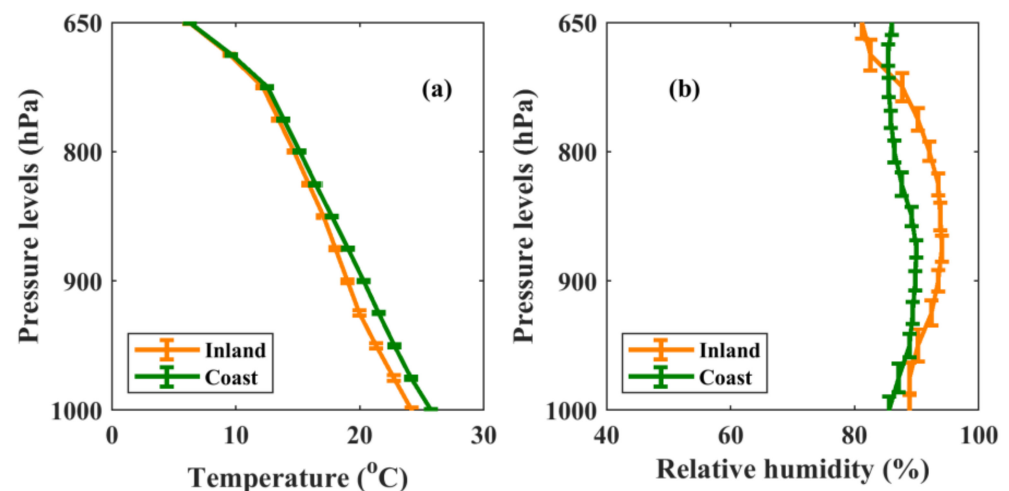


Figure 12. (a) Air temperature ($^{\circ}\text{C}$) and (b) relative humidity (RH%) profiles for the NIO TCs at the coastal and inland stations.

5. Summary and Conclusions

This study concentrated on the NIO TCs' raindrop size distribution (RSD) features measured at the coastal and inland stations using ground-based disdrometers. The NIO TCs at the coastal station have more raindrops of diameter > 1 mm than those at the inland station, resulting in higher D_m and smaller $\log_{10}N_w$ values at the coastal station. The contribution of small drops to rainfall rate is relatively higher in the inland station than the coastal station, and opposite characteristic is noticed for raindrops greater than 1 mm in diameter. When comparing D_m and N_w values of NIO TCs with Pacific Ocean TCs, the NIO TCs have a greater number of small- and mid-size drops. Distributions of D_m and $\log_{10}N_w$ values at the coastal and inland stations in convective and stratiform types have lower D_m and higher $\log_{10}N_w$ values as compared to the continental clusters. The GPM DPR relations assessed for both the coastal and inland stations demonstrated distinctions between these two locations. Furthermore, the rainfall kinetic energy expressed in terms of rainfall rate and remote-sensing radar parameters also exhibited dissimilarities between the coast and inland. The association of relatively higher evaporation rate and intense convection with strong updrafts and downdrafts to the NIO TCs at the coast than inland region resulted in dissimilarities in the RSDs between the two considered sites, which suggests that we ought to adopt region-specific (coast and the inland region) empirical relations while estimating NIO TCs' RSD/rainfall parameters from remote sensing radar and rainfall kinetic energy.

Author Contributions: Conceptualization, B.K.S., J.J. and P.-L.L.; data curation, B.K.S., C.K.U., K.K.R., and M.V.R.; formal analysis, B.K.S., J.J., J.L.L. and W.-Y.C.; funding acquisition, P.-L.L.; investigation, B.K.S. and J.J.; methodology, B.K.S., J.J., P.-L.L., J.L.L. and U.K.; project administration, P.-L.L.; resources, C.K.U., P.-L.L. and K.K.R.; software, P.-L.L.; supervision, P.-L.L. and D.-I.L.; validation, B.K.S., J.J., J.L.L. and W.-Y.C.; visualization, B.K.S., U.K., and J.J.; writing—original draft, B.K.S. and J.J.; writing—review and editing, B.K.S., J.J., C.K.U., P.-L.L., J.L.L., W.-Y.C., D.-I.L. and M.V.R. All authors have read and agreed to the published version of the manuscript.

Funding: We greatly acknowledge the Ministry of Science and Technology (MOST), Taiwan for providing grants to carry out this research work under the grant numbers: MOST 108-2111-M-008-028, MOST 108-2625-M-008-011, MOST 104-2923-M-008-003, MOST 108-2811-M-008-595, MOST 108-2811-M-008-558, MOST 109-2111-M-008-017, MOST 109-2625-M-008-014, MOST 109-2811-M-008-555, MOST 109-2811-M-008-563, and MOST 110-2811-M-008-566.

Institutional Review Board Statement: Not applicable.

Informed Consent Statement: Not applicable.

Acknowledgments: We thank the Indian Meteorological Department (IMD), Govt. of India for providing TCs track information. C.K.U. greatly acknowledges the NCESS, Ministry of Earth Sciences (MoES), Govt. of India for the research facility support. K.K.R. acknowledges the Department of Space, Indian Space Research Organization (ISRO), Govt. of India for granting the research facility at Yogi Vemana University, Andhra Pradesh, India. This research was supported by the Ministry of Science and Technology (grant nos. MOST 104-2923-M-008-003, MOST 108-2111-M-008-028, MOST 108-2625-M-008-011, MOST 109-2111-M-008-017, MOST 109-2625-M-008-014), and it was partially supported by the Earthquake-Disaster and Risk Evaluation and Management Center, E-DREaM, from the Featured Areas Research Center Program within the framework of the Higher Education Sprout Project by the Ministry of Education (MOE) in Taiwan. First author, B.K.S., acknowledges the Ministry of Science and Technology (MOST) for providing the fellowship under the grant numbers: MOST 108-2625-M-008-011, MOST 108-2811-M-008-595 and MOST 109-2811-M-008-563. B.K.S., also acknowledges the Ministry of Earth Sciences (MoES), Govt. of India, for providing the senior research fellowship for the academic years 2010-2013 (during which B.K.S. conducted the RSD measurements at Kadapa) under the grant number MOES/ATMOS/R&D/PIC/001/2008. Second author J.J., carried out this research work under the grant number MOST 108-2811-M-008-558, MOST 109-2811-M-008-555, and MOST 110-2811-M-008-566.

Conflicts of Interest: The authors declare no conflict of interest.

References

1. Liao, L.; Meneghini, R.; Tokay, A. Uncertainties of GPM DPR Rain Estimates Caused by DSD Parameterizations. *J. Appl. Meteorol. Clim.* **2014**, *53*, 2524–2537. [[CrossRef](#)]
2. Wu, Z.; Zhang, Y.; Zhang, L.; Hao, X.; Lei, H.; Zheng, H. Validation of GPM Precipitation Products by Comparison with Ground-Based Parsivel Disdrometers over Jianghuai Region. *Water* **2019**, *11*, 1260. [[CrossRef](#)]
3. Janapati, J.; Seela, B.K.; Lin, P.-L.; Wang, P.K.; Kumar, U. An assessment of tropical cyclones rainfall erosivity for Taiwan. *Sci. Rep.* **2019**, *9*, 15862–15864. [[CrossRef](#)]
4. Steiner, M.; Smith, J.A. Reflectivity, Rain Rate, and Kinetic Energy Flux Relationships Based on Raindrop Spectra. *J. Appl. Meteorol.* **2000**, *39*, 1923–1940. [[CrossRef](#)]
5. Jayalakshmi, J.; Reddy, K.K. Raindrop size distributions of southwest and northeast monsoon heavy precipitation observed over Kadapa (14°4' N, 78°82' E), a semi-arid region of India. *Curr. Sci.* **2014**, *107*, 1312–1320.
6. Krishna, U.V.M.; Reddy, K.K.; Seela, B.K.; Shirooka, R.; Lin, P.-L.; Pan, C.-J. Raindrop size distribution of easterly and westerly monsoon precipitation observed over Palau islands in the Western Pacific Ocean. *Atmospheric Res.* **2016**, *174*, 41–51. [[CrossRef](#)]
7. Seela, B.K.; Janapati, J.; Lin, P.-L.; Wang, P.K.; Lee, M.-T. Raindrop Size Distribution Characteristics of Summer and Winter Season Rainfall Over North Taiwan. *J. Geophys. Res. Atmos.* **2018**, *123*, 11–602. [[CrossRef](#)]
8. Kumar, S.B.; Reddy, K.K. Rain drop size distribution characteristics of cyclonic and north east monsoon thunderstorm precipitating clouds observed over Kadapa (14.47° N, 78.82° E), tropical semi-arid region of India. *Mausam* **2013**, *64*, 35–48.
9. Janapati, J.; Reddy, M.V.; Reddy, K.K.; Lin, P.-L.; Liu, C.-Y. A study on raindrop size distribution variability in before and after landfall precipitations of tropical cyclones observed over southern India. *J. Atmospheric Solar-Terrestrial Phys.* **2017**, *159*, 23–40. [[CrossRef](#)]
10. Chen, Y.; Duan, J.; An, J.; Liu, H. Raindrop Size Distribution Characteristics for Tropical Cyclones and Meiyu-Baiu Fronts Impacting Tokyo, Japan. *Atmosphere* **2019**, *10*, 391. [[CrossRef](#)]
11. Seela, B.K.; Janapati, J.; Lin, P.-L.; Reddy, K.K.; Shirooka, R.; Wang, P.K. A Comparison Study of Summer Season Raindrop Size Distribution Between Palau and Taiwan, Two Islands in Western Pacific. *J. Geophys. Res. Atmos.* **2017**, *122*, 11–787. [[CrossRef](#)]
12. Le Loh, J.; Lee, D.-I.; You, C.-H. Inter-comparison of DSDs between Jincheon and Miryang at South Korea. *Atmospheric Res.* **2019**, *227*, 52–65. [[CrossRef](#)]
13. Seela, B.K.; Reddy, K.K.; Jayalakshmi, J.; Rao, T.N.; Lin, P.-L.; Liu, C.-Y.; Kumar, U. Precipitation and cloud microstructure variations between two southern Indian stations. In *Remote Sensing of the Atmosphere, Clouds, and Precipitation VI, Proceedings of SPIE Asia-Pacific Remote Sensing*; SPIE: New Delhi, India, 2016; Volume 9876, p. 98761. [[CrossRef](#)]
14. Tokay, A.; Short, D.A.; Williams, C.R.; Ecklund, W.L.; Gage, K.S. Tropical Rainfall Associated with Convective and Stratiform Clouds: Intercomparison of Disdrometer and Profiler Measurements. *J. Appl. Meteorol.* **1999**, *38*, 302–320. [[CrossRef](#)]
15. Sumesh, R.; Resmi, E.; Unnikrishnan, C.; Jash, D.; Sreekanth, T.; Resmi, M.M.; Rajeevan, K.; Nita, S.; Ramachandran, K. Microphysical aspects of tropical rainfall during Bright Band events at mid and high-altitude regions over Southern Western Ghats, India. *Atmospheric Res.* **2019**, *227*, 178–197. [[CrossRef](#)]
16. McFarquhar, G.M.; Hsieh, T.-L.; Freer, M.; Mascio, J.; Jewett, B.F. The characterization of ice hydrometeor gamma size distributions as volumes in N–λ–μ phase space: Implications for microphysical process modeling. *J. Atmos. Sci.* **2015**, *72*, 892–909. [[CrossRef](#)]
17. Tokay, A.; Bashor, P.G.; Habib, E.; Kasparis, T. Raindrop Size Distribution Measurements in Tropical Cyclones. *Mon. Weather. Rev.* **2008**, *136*, 1669–1685. [[CrossRef](#)]
18. Janapati, J.; Seela, B.K.; Lin, P.-L.; Wang, P.K.; Tseng, C.-H.; Reddy, K.K.; Hashiguchi, H.; Feng, L.; Das, S.K.; Unnikrishnan, C.K. Raindrop Size Distribution Characteristics of Indian and Pacific Ocean Tropical Cyclones Observed at India and Taiwan Sites. *J. Meteorol. Soc. Jpn.* **2020**, *98*, 299–317. [[CrossRef](#)]
19. Bao, X.; Wu, L.; Tang, B.; Ma, L.; Wu, D.; Tang, J.; Chen, H.; Wu, L. Variable Raindrop Size Distributions in Different Rainbands Associated with Typhoon Fitow (2013). *J. Geophys. Res. Atmos.* **2019**, *124*, 12262–12281. [[CrossRef](#)]
20. Chang, W.-Y.; Wang, T.-C.C.; Lin, P.-L. Characteristics of the Raindrop Size Distribution and Drop Shape Relation in Typhoon Systems in the Western Pacific from the 2D Video Disdrometer and NCU C-Band Polarimetric Radar. *J. Atmospheric Ocean. Technol.* **2009**, *26*, 1973–1993. [[CrossRef](#)]
21. Janapati, J.; Seela, B.K.; Lin, P.-L.; Lee, M.-T.; Joseph, E. Microphysical features of typhoon and non-typhoon rainfall observed in Taiwan, an island in the northwestern Pacific. *Hydrol. Earth Syst. Sci.* **2021**, *25*, 4025–4040. [[CrossRef](#)]
22. Deo, A.; Walsh, K.J.E. Contrasting tropical cyclone and non-tropical cyclone related rainfall drop size distribution at Darwin, Australia. *Atmospheric Res.* **2016**, *181*, 81–94. [[CrossRef](#)]
23. Chen, B.-j.; Wang, Y.; Ming, J. Microphysical characteristics of the raindrop size distribution in Typhoon Morakot (2009). *J. Trop. Meteorol.* **2012**, *18*, 162–171.
24. Radhakrishna, B.; Rao, T.N. Differences in cyclonic raindrop size distribution from southwest to northeast monsoon season and from that of noncyclonic rain. *J. Geophys. Res. Space Phys.* **2010**, *115*, 115. [[CrossRef](#)]
25. Kumari, N.P.A.; Kumar, S.B.; Jayalakshmi, J.; Reddy, K.K. Raindrop size distribution variations in JAL and NILAM cyclones induced precipitation observed over Kadapa (14.47° N, 78.82° E), a tropical semi-arid region of India. *Indian J. Radio Space Phys.* **2014**, *43*, 57–66.

26. Ramanujam, S.; Radhakrishnan, C.; Subramani, D.; Chakravarthy, B. On the Effect of Non-Raining Parameters in Retrieval of Surface Rain Rate Using TRMM PR and TMI Measurements. *IEEE J. Sel. Top. Appl. Earth Obs. Remote Sens.* **2012**, *5*, 735–743. [[CrossRef](#)]
27. Balaji, C.; Krishnamoorthy, C.; Chandrasekar, R. On the possibility of retrieving near-surface rain rate from the microwave sounder SAPHIR of the Megha-Tropiques mission. *Curr. Sci.* **2014**, *106*, 587–593.
28. Suh, S.-H.; Kim, H.-J.; Lee, D.-I.; Kim, T.-H. Geographical Characteristics of Raindrop Size Distribution in the Southern Parts of South Korea. *J. Appl. Meteorol. Clim.* **2021**, *60*, 157–169. [[CrossRef](#)]
29. Harikumar, R. Orographic effect on tropical rain physics in the Asian monsoon region. *Atmospheric Sci. Lett.* **2016**, *17*, 556–563. [[CrossRef](#)]
30. Sumesh, R.K.; Resmi, E.A.; Unnikrishnan, C.K.; Jash, D.; Ramachandran, K.K. Signatures of Shallow and Deep Clouds Inferred from Precipitation Microphysics Over Windward Side of Western Ghats. *J. Geophys. Res. Atmos.* **2021**, *126*. [[CrossRef](#)]
31. Radhakrishna, B.; Rao, T.N.; Rao, D.N.; Rao, N.P.; Nakamura, K.; Sharma, A.K. Spatial and seasonal variability of raindrop size distributions in southeast India. *J. Geophys. Res. Space Phys.* **2009**, *114*, 114. [[CrossRef](#)]
32. Yuter, S.E.; Kingsmill, D.; Nance, L.B.; Löffler-Mang, M. Observations of Precipitation Size and Fall Speed Characteristics within Coexisting Rain and Wet Snow. *J. Appl. Meteorol. Clim.* **2006**, *45*, 1450–1464. [[CrossRef](#)]
33. Löffler-Mang, M.; Joss, J. An Optical Disdrometer for Measuring Size and Velocity of Hydrometeors. *J. Atmospheric Ocean. Technol.* **2000**, *17*, 130–139. [[CrossRef](#)]
34. Battaglia, A.; Rustemeier, E.; Tokay, A.; Blahak, U.; Simmer, C. PARSIVEL Snow Observations: A Critical Assessment. *J. Atmospheric Ocean. Technol.* **2010**, *27*, 333–344. [[CrossRef](#)]
35. Jaffrain, J.; Berne, A. Experimental Quantification of the Sampling Uncertainty Associated with Measurements from PARSIVEL Disdrometers. *J. Hydrometeorol.* **2011**, *12*, 352–370. [[CrossRef](#)]
36. Friedrich, K.; Higgins, S.; Masters, F.J.; Lopez, C.R. Articulating and Stationary PARSIVEL Disdrometer Measurements in Conditions with Strong Winds and Heavy Rainfall. *J. Atmospheric Ocean. Technol.* **2013**, *30*, 2063–2080. [[CrossRef](#)]
37. Tokay, A.; Wolff, D.B.; Petersen, W.A. Evaluation of the New Version of the Laser-Optical Disdrometer, OTT Parsivel2. *J. Atmospheric Ocean. Technol.* **2014**, *31*, 1276–1288. [[CrossRef](#)]
38. Tokay, A.; Petersen, W.A.; Gatlin, P.; Wingo, M. Comparison of Raindrop Size Distribution Measurements by Collocated Disdrometers. *J. Atmospheric Ocean. Technol.* **2013**, *30*, 1672–1690. [[CrossRef](#)]
39. Atlas, D.; Srivastava, R.C.; Sekhon, R.S. Doppler radar characteristics of precipitation at vertical incidence. *Rev. Geophys.* **1973**, *11*, 1–35. [[CrossRef](#)]
40. Ulbrich, C.W. Natural Variations in the Analytical Form of the Raindrop Size Distribution. *J. Clim. Appl. Meteorol.* **1983**, *22*, 1764–1775. [[CrossRef](#)]
41. Kozu, T.; Nakamura, K. Rainfall Parameter Estimation from Dual-Radar Measurements Combining Reflectivity Profile and Path-integrated Attenuation. *J. Atmospheric Ocean. Technol.* **1991**, *8*, 259–270. [[CrossRef](#)]
42. Tokay, A.; Short, D.A. Evidence from Tropical Raindrop Spectra of the Origin of Rain from Stratiform versus Convective Clouds. *J. Appl. Meteorol.* **1996**, *35*, 355–371. [[CrossRef](#)]
43. Bringi, V.N.; Chandrasekar, V.; Hubbert, J.; Gorgucci, E.; Randeu, W.L.; Schoenhuber, M. Raindrop Size Distribution in Different Climatic Regimes from Disdrometer and Dual-Polarized Radar Analysis. *J. Atmospheric Sci.* **2003**, *60*, 354–365. [[CrossRef](#)]
44. Fornis, R.L.; Vermeulen, H.R.; Nieuwenhuis, J.D. Kinetic energy–rainfall intensity relationship for Central Cebu, Philippines for soil erosion studies. *J. Hydrol.* **2005**, *300*, 20–32. [[CrossRef](#)]
45. Dee, D.P.; Uppala, S.M.; Simmons, A.J.; Berrisford, P.; Poli, P.; Kobayashi, S.; Andrae, U.; Balmaseda, M.A.; Balsamo, G.; Bauer, P.; et al. The ERA-Interim reanalysis: Configuration and performance of the data assimilation system. *Q. J. R. Meteorol. Soc.* **2011**, *137*, 553–597. [[CrossRef](#)]
46. Wang, M.; Zhao, K.; Xue, M.; Zhang, G.; Liu, S.; Wen, L.; Chen, G. Precipitation microphysics characteristics of a Typhoon Matmo (2014) rainband after landfall over eastern China based on polarimetric radar observations. *J. Geophys. Res. Atmos.* **2016**, *121*, 12–415. [[CrossRef](#)]
47. Wen, L.; Zhao, K.; Chen, G.; Wang, M.; Zhou, B.; Huang, H.; Hu, D.; Lee, W.-C.; Hu, H. Drop Size Distribution Characteristics of Seven Typhoons in China. *J. Geophys. Res. Atmos.* **2018**, *123*, 6529–6548. [[CrossRef](#)]
48. Chen, B.; Yang, J.; Pu, J. Statistical Characteristics of Raindrop Size Distribution in the Meiyu Season Observed in Eastern China. *J. Meteorol. Soc. Jpn.* **2013**, *91*, 215–227. [[CrossRef](#)]
49. Hu, Z.; Srivastava, R.C. Evolution of Raindrop Size Distribution by Coalescence, Breakup, and Evaporation: Theory and Observations. *J. Atmospheric Sci.* **1995**, *52*, 1761–1783. [[CrossRef](#)]
50. Liao, L.; Meneghini, R. A study of air/space-borne dual-wavelength radar for estimation of rain profiles. *Adv. Atmospheric Sci.* **2005**, *22*, 841–851. [[CrossRef](#)]
51. Mishchenko, M.; Travis, L.D.; Mackowski, D.W. T-matrix computations of light scattering by nonspherical particles: A review. *J. Quant. Spectrosc. Radiat. Transf.* **1996**, *55*, 535–575. [[CrossRef](#)]
52. Brandes, E.A.; Zhang, G.; Vivekanandan, J. Experiments in Rainfall Estimation with a Polarimetric Radar in a Subtropical Environment. *J. Appl. Meteorol.* **2002**, *41*, 674–685. [[CrossRef](#)]
53. Liao, L.; Meneghini, R.; Iguchi, T.; Tokay, A. Characteristics of DSD Bulk Parameters: Implication for Radar Rain Retrieval. *Atmosphere* **2020**, *11*, 670. [[CrossRef](#)]

54. Zeng, Q.; Zhang, Y.; Lei, H.; Xie, Y.; Gao, T.; Zhang, L.; Wang, C.; Huang, Y. Microphysical Characteristics of Precipitation during Pre-monsoon, Monsoon, and Post-monsoon Periods over the South China Sea. *Adv. Atmospheric Sci.* **2019**, *36*, 1103–1120. [[CrossRef](#)]
55. Wu, Z.; Zhang, Y.; Zhang, L.; Lei, H.; Xie, Y.; Wen, L.; Yang, J. Characteristics of Summer Season Raindrop Size Distribution in Three Typical Regions of Western Pacific. *J. Geophys. Res. Atmos.* **2019**, *124*, 4054–4073. [[CrossRef](#)]
56. Wischmeier, W.H.; Smith, D.D. Rainfall energy and its relationship to soil loss. *Trans. Am. Geophys. Union* **1958**, *39*, 285–291. [[CrossRef](#)]
57. Kinnell, P.I.A. Rainfall Intensity-Kinetic Energy Relationships for Soil Loss Prediction1. *Soil Sci. Soc. Am. J.* **1981**, *45*, 153. [[CrossRef](#)]
58. Jayawardena, A.W.; Rezaur, R.B. Measuring drop size distribution and kinetic energy of rainfall using a force transducer. *Hydrol. Process.* **2000**, *14*, 37–49. [[CrossRef](#)]
59. Verstraeten, G.; Poesen, J.; Demarée, G.; Salles, C. Long-term (105 years) variability in rain erosivity as derived from 10-min rainfall depth data for Ukkel (Brussels, Belgium): Implications for assessing soil erosion rates. *J. Geophys. Res. Space Phys.* **2006**, *111*, 111. [[CrossRef](#)]
60. Nanko, K.; Moskalski, S.M.; Torres, R. Rainfall erosivity–intensity relationships for normal rainfall events and a tropical cyclone on the US southeast coast. *J. Hydrol.* **2016**, *534*, 440–450. [[CrossRef](#)]
61. Van Dijk, A.I.J.M.; Meesters, A.G.C.A.; Schellekens, J.; Bruijnzeel, L. A two-parameter exponential rainfall depth-intensity distribution applied to runoff and erosion modelling. *J. Hydrol.* **2005**, *300*, 155–171. [[CrossRef](#)]
62. Mondal, A.; Khare, D.; Kundu, S. Change in rainfall erosivity in the past and future due to climate change in the central part of India. *Int. Soil Water Conserv. Res.* **2016**, *4*, 186–194. [[CrossRef](#)]
63. Sanchez-Moreno, J.F.; Mannaerts, C.M.; Jetten, V.; Löffler-Mang, M. Rainfall kinetic energy–intensity and rainfall momentum–intensity relationships for Cape Verde. *J. Hydrol.* **2012**, *454–455*, 131–140. [[CrossRef](#)]
64. Lim, Y.S.; Kim, J.K.; Kim, J.W.; Park, B.I.; Kim, M.S. Analysis of the relationship between the kinetic energy and intensity of rainfall in Daejeon, Korea. *Quat. Int.* **2015**, *384*, 107–117. [[CrossRef](#)]
65. Iguchi, T.; Seto, S.; Meneghini, R.; Yoshida, N.; Awaka, J.; Kubota, T. *GPM/DPR Level-2 Algorithm Theoretical Basis Document*; NASA Goddard Space Flight Center: Greenbelt, MD, USA, 2010.
66. Skofronick-Jackson, G.; Petersen, W.A.; Berg, W.; Kidd, C.; Stocker, E.F.; Kirschbaum, D.B.; Kakar, R.; Braun, S.A.; Huffman, G.J.; Iguchi, T.; et al. The Global Precipitation Measurement (GPM) Mission for Science and Society. *Bull. Am. Meteorol. Soc.* **2017**, *98*, 1679–1695. [[CrossRef](#)] [[PubMed](#)]
67. Rosenfeld, D.; Ulbrich, C.W. Cloud Microphysical Properties, Processes, and Rainfall Estimation Opportunities. *Meteorol. Monogr.* **2003**, *52*, 237–258. [[CrossRef](#)]
68. Atlas, D.; Ulbrich, C.W.; Marks, F.D., Jr.; Black, R.A.; Amitai, E.; Willis, P.T.; Samsury, C.E. Partitioning tropical oceanic convective and stratiform rains by draft strength. *J. Geophys. Res. Space Phys.* **2000**, *105*, 2259–2267. [[CrossRef](#)]